Zero- and one-dimensional magnetic traps for quasiparticles in diluted magnetic semiconductors

P. Redliński,[1] T. Wojtowicz,[1,2] T. G. Rappoport,[3] A. Libál,[1] J. K. Furdyna,[1] and B. Jankó[1]
[1]*Department of Physics, University of Notre Dame, Notre Dame, Indiana 46556, USA*
[2]*Institute of Physics, Polish Academy of Sciences, 02-668 Warsaw, Poland*
[3]*Instituto de Física, Universidade Federal do Rio de Janeiro, Caixa Postale 88528, 21945-970 Rio de Janeiro RJ, Brazil*
(Received 23 February 2005; published 3 August 2005)

We investigate the possibility of trapping quasiparticles in hybrid structures composed of a magnetic quantum well placed a few nanometers below a ferromagnetic micromagnet. We are interested in two different micromagnet shapes: cylindrical (microdisk) and rectangular geometry. We show that in the case of a microdisk, the quasiparticles are localized in all three directions and therefore zero-dimensional states are created. In the case of an elongated rectangular micromagnet the quasiparticles can move freely in one direction, hence one-dimensional states are formed. After calculating the magnetic field profiles produced by the micromagnets, we analyze in detail the light absorption spectrum for different micromagnet thicknesses and different distances between the micromagnet and the semimagnetic quantum well. We argue that the discrete spectrum of the localized states can be detected via spatially resolved low-temperature optical measurement.

DOI: 10.1103/PhysRevB.72.085209 PACS number(s): 75.50.Pp, 78.67.De, 78.40.Fy

I. INTRODUCTION

Currently, there is an increasing interest in using the spin of particles, in addition to their charge, as the basis for new types of "spin electronics."[1–3] In this work we show that the spin degrees of freedom can be utilized for achieving spatial localization of charged quasiparticles (electrons, holes, or trions[4,5]), as well as of neutral complexes, such as excitons.[4,6]

In this paper we consider a hybrid structure consisting of a CdMnTe/CdMgTe quantum well (QW) structure at a small, but finite distance from a ferromagnetic micromagnet. Due to the Zeeman interaction, the inhomogeneous magnetic field produced by the micromagnet acts as an effective potential that can "trap" spin polarized quasiparticles in the QW. In this paper we explore two specific types of micromagnets: one with cylindrical[7] and one with rectangular[8–10] symmetry. In both cases the thickness of the micromagnets is of the order of a few hundreds of nanometers and their lateral dimension is of the order of microns. We will show that in both geometries the micromagnets are very effective in localizing quasiparticles. For the microdisk, the quasiparticles are localized below the center of the disk in all three spatial directions. For the rectangular micromagnet, the quasiparticles are localized below the poles of the ferromagnet and the localization occurs only in two spatial dimensions. Thus in the latter case the quasiparticles can move quasifreely in one direction.

The choice of the diluted magnetic semiconductor (CdMnTe) QW instead of the classical one (i.e., CdTe) is motivated by the desire to achieve more efficient spin traps, leading to clear localization effects. Related phenomena and spintronic applications have recently been explored in magnetic semiconductor/superconductor hybrid structures.[11] In diluted magnetic semiconductor (DMS) materials the exchange interaction between delocalized band electrons and localized magnetic ions (Mn^{++} ions in the case at hand) leads to a splitting between band states for different spin components (for a review of relevant properties of DMS see Ref. 12). The so-called giant Zeeman spin splitting has been extensively investigated in the 1980s in II-VI based DMSs.[13] A consequence of this effect is the huge effective g factor for most DMS materials. For example, Dietl[14] *et al.* reported an electron g factor of about 500 in a sub-Kelvin experiment in a CdMnSe, which implies a value of about 2000 for the g factor of a hole in this material. According to our previous calculations[10] such values for the effective g factors can in fact result in the confinement of quasiparticles in a small lateral region inside QW. The actual details of the optical response will depend in a sensitive way on the values of the electron and hole g factors. Our focus on QW structures instead of normal films has both experimental and theoretical motivations. From the experimental point of view, we would like to avoid the complications caused by the metal-DMS interface. To satisfy this criterion, the QW should be placed at a finite distance from the micromagnet. However, the local magnetic field inside the QW diminishes as the distance d between the micromagnet and the QW increases. Thus, we need to compromise in the value of d in order to have a high magnetic field in the QW and, at the same time, to avoid interface contamination effects. There are also two theoretical motivations that require the QW to be relatively narrow. First, because of the quantum confinement, the heavy and light hole states (degenerate in the bulk at the Γ point) become nondegenerate in the QW geometry. This means that the low-energy absorption spectrum is simplified for the QW. Second, in the narrow QW we can assume that the local magnetic field is uniform throughout the width of the QW, which again simplifies the calculation. On the other hand, for practical reasons the QW cannot be too narrow, since the linewidth of the optical resonances increases[15] with decreasing width of the QW (L_{QW}).

In Fig. 1 we present a schematic sketch of the energy states in a DMS QW that can be used for discussing the presence of ferromagnetic micromagnet on the top of the quantum structure. The QW is grown in the [001] direction, chosen here as the $\hat{z}$ axis. Without the micromagnet, the main

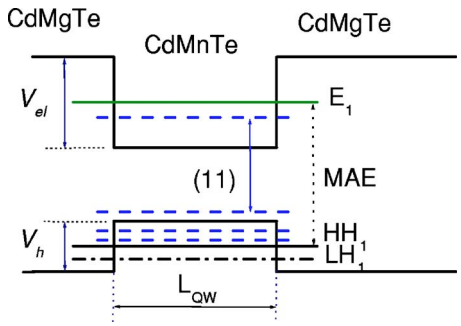

FIG. 1. (Color online) In the absence of a micromagnet we expect the main absorption edge (MAE) between heavy hole (HH_1) and electron (E_1) energy states (full lines). Both energy states show twofold spin degeneracy without external magnetic field. After the deposition of the micromagnet, new states appear below the E_1 state and above the HH_1 state (dashed lines). The spin degeneracy is lifted in each new energy state. In a QW structure the heavy hole states and the light hole states (e.g., HH_1 and LH_1) are split even without external magnetic field.

absorption edge is observed between the states of the heavy hole HH_1 (with a pseudospin of $-3/2$ in units of $\hbar$) and the electron E_1 (with a spin of $-1/2$) with a σ_+ circularly polarized light. In the absence of magnetic field, E_1 and HH_1 are twofold degenerate with respect to the spin, and the first optical transition in the σ_- polarization is at the same energy as for the σ_+ transition. After depositing the micromagnet, we expect that new states will appear below E_1 and above HH_1. These new states are no longer spin degenerate, since the presence of a local magnetic field lifts the Kramers degeneracy. It is important to note that the spin of the states below E_1 remains $-1/2$, and above HH_1 states the spin maintains a pseudospin of $-3/2$. Our main prediction is the following: the experimentally observable transitions between these new states will appear in the absorption or photoluminescence spectrum below the main absorption edge and will be active for σ_+ circularly polarized light.[16] We will focus on the optical absorption, because it provides a mapping of all states. Our results, however, are equally well suited for photoluminescence experiments.

This paper is organized as follows: In Sec. II we present the general theoretical approach and analyze the g-factor anisotropy of the hole states. In Sec. III A we show the results obtained for the absorption coefficient of the microdisk/semiconductor QW structure as a function of a few key parameters, and in Sec. III B we present the analysis for the rectangular micromagnet/semiconductor QW structure. Finally, we present a detailed discussion and explore the experimental consequences of our results.

II. THE THEORETICAL MODEL

The goal of this section is to derive effective Hamiltonians for both micromagnet geometries. We begin by considering separately the electron in the valence band and in the conduction band. We then discuss the Zeeman interaction between the local magnetic field produced by the micromagnet and the quasiparticle spin. At the end of this section we discuss the experimentally observed anisotropy of the hole g factor (g_h).

Our starting point is the Luttinger Hamiltonian[17] H_L of the valence electron in the k representation (note that we are working in the *electron* representation of the valence band), within the base of the four-component spinor $\Psi^\dagger = (\Psi^*_{+3/2}, \Psi^*_{-1/2}, \Psi^*_{+1/2}, \Psi^*_{-3/2})$,

$$H_L = \begin{pmatrix} H^a & H^b \\ H^{b*} & {}^T H^a \end{pmatrix}, \tag{1}$$

where the matrices H^a and H^b can be written schematically as

$$H^a = \begin{pmatrix} H_h & -c \\ -c & H_l \end{pmatrix}, \tag{2}$$

$$H^b = \begin{pmatrix} -b & 0 \\ 0 & b \end{pmatrix}, \tag{3}$$

and where $c = (-\hbar^2/2m_0)\sqrt{3}[\gamma_2(k_x^2 - k_y^2) - 2i\gamma_3 k_x k_y]$ and $b = (-\hbar^2/2m_0)2\sqrt{3}\gamma_3 k_z(k_x - ik_y)$. The symbol ${}^T H^a$ denotes the H^a matrix with interchanged *diagonal* elements. Note that b is proportional to k_z, a property that we will use later in the discussion. The OX, OY, and OZ axis correspond to the [1,0,0], [0,1,0], and [0,0,1] crystallographic directions and the spin is quantized along [0,0,1]. Using the substitution $\vec{k} \Rightarrow -i\vec{\nabla}$, the Hamiltonian in the $\vec{k}$ representation is transformed to the $\vec{r}$ representation.

Now we consider the QW structure. We choose our four-component spinor wave function in the following form:

$$\Psi(\vec{r}) = \begin{pmatrix} \Psi_{3/2}(\vec{r}) \\ \Psi_{-1/2}(\vec{r}) \\ \Psi_{1/2}(\vec{r}) \\ \Psi_{-3/2}(\vec{r}) \end{pmatrix} = \begin{pmatrix} f_h(z)\phi_{+3/2}(x,y) \\ f_l(z)\phi_{-1/2}(x,y) \\ f_l(z)\phi_{+1/2}(x,y) \\ f_h(z)\phi_{-3/2}(x,y) \end{pmatrix}, \tag{4}$$

where $\phi(x,y)$'s are not yet determined, and $f_h(z)$ and $f_l(z)$ are ground-state functions of the following set of Schrödinger eigenequations,

$$\left(\frac{\hbar^2(\gamma_1 - 2\gamma_2)}{2m_0}\frac{d^2}{dz^2} + V^h_{QW}(z)\right) f_h(z) = \epsilon_h f_h(z), \tag{5}$$

$$\left(\frac{\hbar^2(\gamma_1 + 2\gamma_2)}{2m_0}\frac{d^2}{dz^2} + V^h_{QW}(z)\right) f_l(z) = \epsilon_l f_l(z), \tag{6}$$

where ϵ_h and ϵ_l are the ground-state energies. In Eqs. (5) and (6) $m_0/(\gamma_1 - 2\gamma_2)$ and $m_0/(\gamma_1 + 2\gamma_2)$ are the z components of heavy hole and light hole effective masses and $V^h_{QW}(z)$ is a potential energy of the QW coming from discontinuity of the edge of the valence band. We assume this potential to be rectangular (see Fig. 1),

$$V^h_{QW}(z) = \begin{cases} 0 & \text{for } |z| < L_{QW}/2 \\ -V_h & \text{for } |z| > L_{QW}/2. \end{cases} \tag{7}$$

The functions $f_h(z)$ and $f_l(z)$ that satisfy Eqs. (5) and (6) are real-valued even functions fulfilling the relation $\int f_h^*(z) p_z f_l(z) dz = 0$. These properties of f_h and f_l can be used

as follows: In the subspace of Hilbert space spanned by our trial wave function H_L, Eq. (1) is written as a new 4×4 matrix $\tilde{H}_L$,

$$\tilde{H}_L = \begin{pmatrix} \tilde{H}^a & \tilde{H}^b \\ \tilde{H}^b & {}^T\tilde{H}^a \end{pmatrix}, \tag{8}$$

where

$$\tilde{H}^a = \begin{pmatrix} H_h & -cI_{hl} \\ -cI_{hl}^* & H_l \end{pmatrix}, \tag{9}$$

and

$$\tilde{H}^b = \begin{pmatrix} 0 & 0 \\ 0 & 0 \end{pmatrix}. \tag{10}$$

I_{hl} in Eq. (9) is the overlap integral, defined by $I_{hl} \equiv \int f_h^*(z) f_l(z) dz$. We can write the matrix $\tilde{H}^b$ in the form given by Eq. (10), as the term b in (3) reduces to zero because of the relation $\int f_h^*(z) p_z f_l(z) dz = 0$. Furthermore, in the $\vec{r}$ representation the two quantities H_h and H_l in the matrix $\tilde{H}^a$ take the following form:

$$H_h = \frac{\hbar^2}{2m_0}(\gamma_1 + \gamma_2)\left(\frac{d^2}{dx^2} + \frac{d^2}{dy^2}\right) + \epsilon_h, \tag{11}$$

$$H_l = \frac{\hbar^2}{2m_0}(\gamma_1 - \gamma_2)\left(\frac{d^2}{dx^2} + \frac{d^2}{dy^2}\right) + \epsilon_l, \tag{12}$$

and

$$c = \frac{\hbar^2}{2m_0}\sqrt{3}\left[\gamma_2\left(\frac{d^2}{dx^2} - \frac{d^2}{dy^2}\right) - 2i\gamma_3 \frac{d}{dx}\frac{d}{dy}\right]. \tag{13}$$

After making these approximations the wave function $\tilde{\Psi}$ satisfying $\tilde{H}_L\tilde{\Psi} = E_h\tilde{\Psi}$ has only two nonvanishing components,

$$\tilde{\Psi}(\vec{r}) = \begin{pmatrix} \phi_{+3/2}(x,y) \\ \phi_{-1/2}(x,y) \\ 0 \\ 0 \end{pmatrix} \tag{14}$$

and

$$\tilde{\Psi}(\vec{r}) = \begin{pmatrix} 0 \\ 0 \\ \phi_{+1/2}(x,y) \\ \phi_{-3/2}(x,y) \end{pmatrix}. \tag{15}$$

The Zeeman interaction due to the local magnetic field produced by the micromagnet mixes both states and lifts their degeneracy.

Now we consider the conduction band. We assume that the dispersion relation of the conduction electron is parabolic

$$H_e = E_G - \frac{\hbar^2}{2m_0}\gamma_{el}\left(\frac{d^2}{dx^2} + \frac{d^2}{dy^2} + \frac{d^2}{dz^2}\right) + V_{QW}^{el}(z), \tag{16}$$

where E_G is the energy gap of a QW, m_0/γ_{el} is the electron effective mass, and V_{QW}^{el} is the potential energy coming from the discontinuity of the conduction band (see Fig. 1)

$$V_{QW}^{el}(z) = \begin{cases} 0 & \text{for } |z| < L_{QW}/2 \\ V_{el} & \text{for } |z| > L_{QW}/2 \end{cases}. \tag{17}$$

For the electron we assume the following factorized trial wave function:

$$\Psi_{el} = \begin{pmatrix} f_{el}(z)\phi_+(x,y) \\ f_{el}(z)\phi_-(x,y) \end{pmatrix}, \tag{18}$$

where the function $f_{el}(z)$ is the solution of the one-dimensional Schrödinger equation

$$\left(-\frac{\hbar^2\gamma_{el}}{2m_0}\frac{d^2}{dz^2} + V_{QW}^{el}(z)\right) f_{el}(z) = \epsilon_{el} f_{el}(z). \tag{19}$$

Both functions $\phi_\pm$ fulfill the following eigenequation:

$$\tilde{H}_e\phi_\pm(x,y) \equiv \left[-\frac{\hbar^2\gamma_{el}}{2m_0}\left(\frac{d^2}{dx^2} + \frac{d^2}{dy^2}\right) + \epsilon_{el}\right]\phi_\pm(x,y) = E_e\phi_\pm(x,y). \tag{20}$$

The Zeeman Hamiltonian used for both the conduction and the valence electrons can be written as

$$H_Z(\vec{r}) = \mu_B \vec{s}\hat{g}_{eff}\vec{B}(\vec{r}), \tag{21}$$

where $\hat{g}_{eff}$ is a tensor, μ_B is the Bohr magneton, $\vec{B}(\vec{r})$ is the local magnetic field produced by the micromagnet, and $\vec{s}$ is the spin-$\frac{1}{2}$ operator. For the conduction band $\hat{g}_{eff} = g_e\hat{1} \equiv \mathrm{diag}(g_e, g_e, g_e)$ and for valence electron $\hat{g}_{eff} = g_h\hat{1} \equiv \mathrm{diag}(g_h, g_h, g_h)$, where $\hat{1}$ is the 3×3 identity matrix. For the conduction electron, the spin-$\frac{1}{2}$ operator in the basis of the Bloch states is a 2×2-matrix proportional to the Pauli matrices. For the valence electron the spin operator is a 4×4-matrix, as shown in Ref. 18. In addition to the previous approximations we assume that the QW is narrow, and we rewrite Eq. (21) as

$$\tilde{H}_Z(x,y) = \mu_B \vec{s}\hat{g}_{eff}\vec{B}(x,y,z=d), \tag{22}$$

where d is the distance between the QW and the micromagnet.

Summarizing, the original Hamiltonians were transformed into the two-dimensional effective Hamiltonians of the valence ($\mathcal{H}_h$) and of the conduction electron ($\mathcal{H}_e$)

$$\mathcal{H}_h(x,y) = \tilde{H}_L(x,y) + \tilde{H}_Z(x,y), \tag{23}$$

$$\mathcal{H}_e(x,y) = \tilde{H}_e(x,y) + \tilde{H}_Z(x,y). \tag{24}$$

The procedure for diagonalizing these Hamiltonians is as follows: first, the magnetic field produced by the micromagnet is calculated by solving the magnetostatic Maxwell equations,[19] either by using a magnetization distribution determined from micromagnetic simulations[7] (in the case of the disk) or by assuming that the micromagnet can be represented by a uniformly magnetized domain (in the case of rectangular micromagnet). Then, the electronic spectrums of the conduction band and the valence band are calculated by

approximating the Schrödinger eigenequations with finite difference algebraic equations. In the case of the microdisk, the algebraic equations are generated on a two-dimensional grid and Eqs. (23) and (24) are solved directly. In the case of the rectangular micromagnet—because of its large elongation in the y direction ($D_y=2$ μm)—we can make the ansatz that the quasiparticle is free to move in this direction so the plane wave form of the wave function is assumed in y direction. Thus, in the case of a rectangular micromagnet the finite difference equations are generated only on a one-dimensional grid.

Given the calculated eigenvalues and eigenfunctions, we use Fermi's golden rule to obtain the absorption coefficient[16]

$$\alpha_{\pm}(\omega) \simeq \frac{1}{\omega}\sum_{i,j} |\langle e_j|p_x \pm ip_y|h_i\rangle|^2 \delta[\hbar\omega - (E_{e_i} - E_{h_i})], \tag{25}$$

where $\{|e_i\rangle, E_{e_i}\}$ and $\{|h_j\rangle, E_{h_j}\}$ are the eigensolutions of the conduction band and valence band Hamiltonians, $\mathcal{H}_e$ and $\mathcal{H}_h$, respectively. The Coulomb interaction between the electrons and the holes leads to the creation of long-lived excitons, which in turn generate sharp individual optical lines. We assumed that the exciton states are formed and that the MAE corresponds to the $1S$ exciton transition in the QW without the micromagnet. In the following figures we have taken the zero energy at the $1S$ exciton main absorption peak. To create the final spectrum, each optical line we calculate is broadened by a Gaussian function with a linewidth of 1 meV. This is a reasonable approximation for a typical experimental resolution.

Anisotropy of the hole g factor

The Zeeman splitting of the valence band edge depends on the direction of the magnetic field with respect to the growth direction of the quantum well.[20] In order to demonstrate this we consider two configurations: a constant magnetic field parallel to the plane of the quantum well, $\vec{B}=B\vec{e}_x$; and a constant magnetic field perpendicular to this plane, $\vec{B}=B\vec{e}_z$.

Starting with $\vec{B}=B\vec{e}_z$, we find it convenient to use a different basis than that used in the previous part of the paper: the new basis vectors are $\Psi^{\dagger}=(\Psi^*_{+3/2}, \Psi^*_{-3/2}, \Psi^*_{+1/2}, \Psi^*_{-1/2})$. In this new basis, the Luttinger Hamiltonian, Eq. (1) or Eq. (8), for the edge of the valence band in the QW is a diagonal matrix

$$H = \begin{pmatrix} +\frac{1}{2}g_h\mu_B B & 0 & 0 & 0 \\ 0 & -\frac{1}{2}g_h\mu_B B & 0 & 0 \\ 0 & 0 & -\Delta_{lh} + \frac{1}{6}g_h\mu_B B & 0 \\ 0 & 0 & 0 & -\Delta_{lh} - \frac{1}{6}g_h\mu_B B \end{pmatrix}, \tag{26}$$

where the energy splitting $\Delta_{lh}=|E_l - E_h|$ is caused by the quantum well confinement. This splitting is also present in structures under strain and it can be either positive or negative as shown in Ref. 18. Looking at the Hamiltonian H, Eq. (26), we can see that the energy of the heavy hole $\left(+\frac{3}{2}, -\frac{3}{2}\right)$ splits by $|g_h\mu_B B|$, whereas the energy of the light hole $\left(+\frac{1}{2}, -\frac{1}{2}\right)$ splits by $|\frac{1}{3}g_h\mu_B B|$, an amount smaller by a factor of 3.

In order to analyze the second geometry ($\vec{B}=B\vec{e}_x$), we write the Hamiltonian for the valence band edge in a QW as follows:

$$H = \begin{pmatrix} \mathbf{0} & \mathbf{0} & \frac{1}{2\sqrt{3}}g_h\mu_B B & 0 \\ \mathbf{0} & \mathbf{0} & 0 & \frac{1}{2\sqrt{3}}g_h\mu_B B \\ \frac{1}{2\sqrt{3}}g_h\mu_B B & 0 & \mathbf{-\Delta_{lh}} & \mathbf{\frac{1}{3}g_h\mu_B B} \\ 0 & \frac{1}{2\sqrt{3}}g_h\mu_B B & \mathbf{\frac{1}{3}g_h\mu_B B} & \mathbf{-\Delta_{lh}} \end{pmatrix}. \tag{27}$$

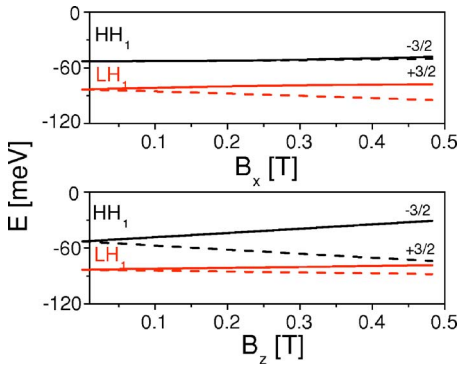

FIG. 2. (Color online) Top panel: splitting of the heavy hole (HH_1) and light hole (LH_1) edges at the Γ point in a QW vs B_x (we use the electron representation). B_y and B_z are set to zero. Bottom panel: splitting of the heavy hole and light hole edges in a QW vs B_z (B_x=0 and B_y=0). Solid and dashed lines represent states with opposite spin. Heavy hole states $\mp 3/2$ *do not split* when the magnetic field is applied in the plane of the QW as seen on the upper panel.

If we omit the mixing between the heavy and light holes [i.e., if we retain only the bold elements in Eq. (27)] then the heavy holes do not split, and the light holes split by $|\frac{2}{3}g_h\mu_B B|$. We note that the light hole splitting is now two times larger than in the case of the perpendicular magnetic field, $\vec{B}=B\vec{e}_z$, where it was $|\frac{1}{3}g_h\mu_B B|$. Solving the eigenvalue problem with Hamiltonian H in Eq. (27), we obtain four solutions as a function of the external magnetic field (see Fig. 2)

$$E_h^{\mp} = -\frac{\Delta_{lh}}{2} \mp \frac{g_h\mu_B B}{6} + \frac{1}{6}\sqrt{9\Delta_{lh}^2 \pm 6\Delta_{lh}g_h\mu_B B + 4(g_h\mu_B B)^2}, \tag{28}$$

$$E_l^{\mp} = -\frac{\Delta_{lh}}{2} \mp \frac{g_h\mu_B B}{6} - \frac{1}{6}\sqrt{9\Delta_{lh}^2 \pm 6\Delta_{lh}g_h\mu_B B + 4(g_h\mu_B B)^2}. \tag{29}$$

When the QW splitting $\Delta_{lh} \gg |g_h\mu_B B|$ then up to terms quadratic in the external field B, Eqs. (28) and (29) can be further simplified to

$$E_h^{\mp} \approx \frac{1}{12}\frac{g_h\mu_B B}{\Delta_{lh}} g_h\mu_B B, \tag{30}$$

$$E_l^{\mp} \approx -\Delta_{lh} \mp \frac{g_h\mu_B B}{3} - \frac{1}{12}\frac{g_h\mu_B B}{\Delta_{lh}} g_h\mu_B B. \tag{31}$$

Because the heavy hole does not split, we are left with three solutions out of the four. In this approximation the energy level of the heavy hole $E_h^{\mp}$ is twofold degenerate and the light hole splits by an amount proportional to the magnetic field $(\frac{2}{3}|\mu_B g_h B|)$, as seen in Eq. (31). These different behaviors can be compared in Fig. 2 where we plotted exact values of $E_h^{\pm}$ and $E_l^{\mp}$ using Eqs. (28) and (29).

In other words, we can say that in a QW, the g_h factor of the first heavy hole states HH_1 is highly anisotropic. Consequently, in the Zeeman term given by Eqs. (21) and (22), the tensor $\hat{g}_h$=diag(g_h, g_h, g_h) can be approximated by $\hat{g}_h \approx$ diag$(0, 0, g_h)$. Indeed, only the component of the field parallel to the growth direction of the QW splits the HH_1 states. The anisotropy that appears naturally using the Luttinger Hamiltonian in the QW is observed experimentally.[20] We compared the results of the optical response for both isotropic and anisotropic g factors and found that absorption spectra are similar, especially in the low-energy region of the spectrum. This result is presented in Sec. III.

III. RESULTS AND DISCUSSION

For the calculations involving both cylindrical and rectangular micromagnets, the following set of Luttinger parameters and electron mass was chosen for both the QW and the barriers: γ_1=4.14, γ_2=1.09, γ_3=1.62, $m_e=m_0/\gamma_e=0.096m_0$. From Eq. (11), the heavy hole effective mass in the plane is $m_0/(\gamma_1+\gamma_2)=0.19m_0$ and the light hole effective mass in the plane is equal to $m_0/(\gamma_1-\gamma_2)=0.33m_0$. A total discontinuity of bands V_T=500 meV, and valence band offset vbo=0.4 is assumed, which corresponds to a discontinuity in the valence band of $V_h=V_T\ vbo$=200 meV, and a discontinuity in the conduction band of $V_{el}=V_T\,(1-vbo)$=300 meV (see Fig. 1). We also choose a quantum well width of L_{QW}=20 Å, for which the splitting between the heavy hole HH_1 and the light hole LH_1 energy states is $\Delta_{lh}\approx$50 meV. Note that there is only one bound heavy hole state and only one bound light hole state for these parameters.

A. Cylindrical micromagnet: A zero-dimensional trap

We investigate a Fe microdisk (with a diameter of R =1 μm, a thickness D_z=50 nm, and $\mu_0 M_s$=2.2 T) in the vortex state.[7,21] In this state, due to the competition between the exchange energy and the demagnetization energy, the magnetization lies in the plane of the microdisk except near the center, where the local magnetization points out of the plane (to reduce the exchange energy), and forms a magnetic vortex. The diameter of the core (R_c), to which the nonzero perpendicular magnetization is confined, extends over only about 60 nm, as previously calculated.[7] It is important to mention that only the z component M_z of the total magnetization $\vec{M}$ produces the "spike" in the magnetic field $\vec{B}$, which traps the quasiparticles.

The magnetic field $\vec{B}$ can be calculated using the magnetization profile of the vortex[7,21] and the magnetostatic Maxwell equations. In Fig. 3 we show the distribution of the magnetic field $\vec{B}(x,y,d)$ in the XY plane at a distance d above the micromagnet, where d is the separation between the micromagnet and the QW. In the magnetostatic picture, the magnetic field $\vec{B}$ is produced by two magnetic charges (of diameter R_c) on two surfaces of the micromagnet. These magnetic charges are separated by a thickness of the micromagnet, D_z. At a distance d=10 nm above the micromagnet, the maximum value of the magnetic field is $|\vec{B}|_{\max}$=0.46 T. The field is nonzero over a distance of 60 to 80 nm from the center of the disk, as shown in Fig. 3. Such a strongly local-

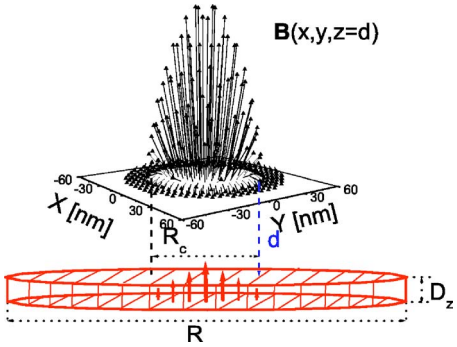

FIG. 3. (Color online) Three-dimensional image of the magnetic field $B(x,y,z=d)$ on the XY surface at a distance d above Fe microdisk. It is assumed that the micromagnet is in the vortex state. The diameter of the region where the z component of the magnetization M_z is nonzero (the core region) is of the order of $R_c=60$ nm, whereas the diameter of the microdisk R is 1 μm, and the thickness of the disk D_z is 50 nm. M_z, depicted by vertical arrows in the core region, is very well approximated by a parabolic profile.

ized magnetic field in both x and y directions, together with the QW confinement results in a quasiparticle localization in all three directions. The particle is localized below the center of the microdisk. We will refer to this system as a zero-dimensional trap.

In Fig. 4 we show the absorption coefficient for three distances d between the microdisk and the QW: $d=5$ nm, 10 nm, and 15 nm. The energy of the photon is measured relative to the energy of the main absorption peak in the QW in the absence of a micromagnet (see Fig. 1). Vertical bars represent the optical oscillator strengths of the transitions, and the numbers $(n_c n_v)$ show that the corresponding line is a transition between the n_v^{th} hole state and the n_c^{th} electron state. The eigenenergies of the conduction electron fulfill $E_1<E_2<\cdots<E_{n_c}<\cdots$ where E_1 is the ground state of the conduction band electron. Eigenenergies of the valence electron obey $E_1>E_2>\cdots>E_{n_v}>\cdots$ where E_1 is the ground state of the valence band electron.

The absorption line was obtained after broadening the δ distribution of each transition, Eq. (25), with a Gaussian function (the linewidth of each resonance is $w=1$ meV). As

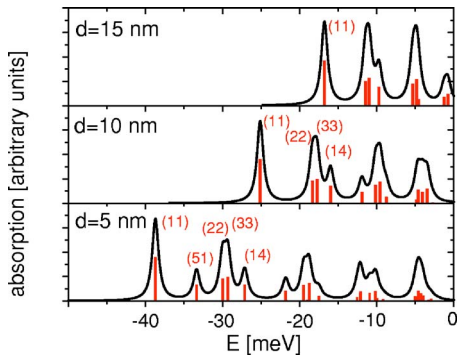

FIG. 4. (Color online) Absorption coefficient for three distances d between the microdisk and the QW with $D_z=50$ nm. The number $(n_c n_v)$ corresponds to transitions between the n_c^{th} electron state and the n_v^{th} hole state.

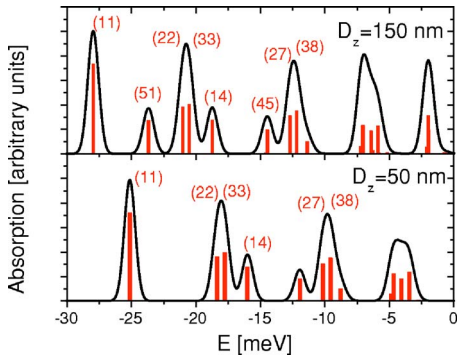

FIG. 5. (Color online) Absorption coefficient for two thicknesses D_z of the ferromagnetic microdisk. In magnetostatic language, D_z is the distance between magnetic charges. The separation between the microdisk and the QW was set to $d=10$ nm.

expected, the peaks shift to lower energies with decreasing d, as the maximum value of B, and thus the effective "potential," are larger for smaller d. At $d=10$ nm, the shift between the (11) transition and the main absorption peak is around 25 meV (we will call this quantity the *binding energy*). As is seen in Fig. 4, the first transition (11) is the most intense, but we can see that nondiagonal transitions, such as (14), also have a relatively large spectral weight. We also see that for the set of parameters we used in our calculation the two closely lying lines (22) and (33) merge into a single large peak in the absorption spectrum.

In Fig. 5 we show the absorption coefficient for two different thicknesses D_z of the microdisk and a value of d fixed at 10 nm. When the thickness D_z increases from 50 nm to 150 nm, the binding energy increases from 25 meV to 28 meV. The transition (51), not seen for $d=10$ nm in Fig. 4, now becomes visible at $D_z=150$ nm. On the other hand, increasing D_z to larger values does not change the absorption substantially, because the separation between magnetic charges (D_z) begins to exceed the dimension of the magnetic charge (R_c).

To get further insight into the optical transitions we follow the prescription defined in Ref. 7 and write the conduction electron two-component spinor as

$$\psi_{m,k}^{c}=f_{el}(z)e^{im\phi}\begin{pmatrix} e^{-i\phi}g_{m,k}^{\uparrow}(\rho) \\ g_{m,k}^{\downarrow}(\rho) \end{pmatrix}, \tag{32}$$

where $m=0,\pm1,\pm2,\ldots$ is the angular momentum quantum number, $k=0,1,2\ldots$ is the radial quantum number and we used cylindrical coordinates (ρ,ϕ,z). This form of the angular dependence of the wave function is exact for electrons described by spherically symmetric bands with quadratic dispersion. Assuming that the valence band can also be approximated by a quadratic dispersion, the hole four-component spinor has the following form:

TABLE I. Mapping of the quantum number n that was used in Fig. 4 and Fig. 5 to described hole states on the (m,k) pairs. Only four states, $n=1,\ldots,4$, which fulfill $E_1>E_2>E_3>E_4$, are mapped, and E_1 is the ground state of the electron in the valence band.

n_v	m	k
1	0	0
2	−1	0
3	+1	0
4	0	1

$$\psi^v_{m,k}=e^{im\phi}\begin{pmatrix} f_h(z)e^{-3i\phi}g^{+3/2}_{m,k}(\rho) \\ f_l(z)e^{-2i\phi}g^{+1/2}_{m,k}(\rho) \\ f_l(z)e^{-i\phi}g^{-1/2}_{m,k}(\rho) \\ f_h(z)g^{-3/2}_{m,k}(\rho)\end{pmatrix}. \quad (33)$$

The dominant part of the electron and the hole wave function calculated in our approach is of the form given in Eqs. (32) and (33).

In Ref. 7 the intraband optical transitions of the conduction band were studied. Selection rules for this type of the transitions imply that the angular momentum quantum number of the envelope wave function m must be changed by ±1 in $\sigma_\pm$ polarizations ($\Delta m=\pm1$). On the other hand for interband transitions $\Delta m=0$ because the initial and the final Bloch states are of different symmetry: the initial state is of P symmetry and the final state is of S symmetry. In order to calculate the σ_+ absorption coefficient using Eq. (25) we have to calculate two integrals: $\langle\Psi_{-3/2}|\Psi_\downarrow\rangle$ and $\langle\Psi_{-1/2}|\Psi_\uparrow\rangle$. Using Eqs. (32) and (33) as an approximation for the true wave function we have

$$\langle\Psi_{-3/2}|\Psi_\downarrow\rangle\approx\int e^{-im\phi}[f_h(z)g^{-3/2}_{m,k}(\rho)]^* f_{el}(z)e^{im'\phi}g^{\downarrow}_{m',k'} \times(\rho)d\phi rdrdz\sim\delta_{m,m'},$$

$$\langle\Psi_{-1/2}|\Psi_\uparrow\rangle\approx\int e^{-im\phi}[f_h(z)g^{-1/2}_{m,k}(\rho)]^* f_{el}(z)e^{im'\phi}g^{\uparrow}_{m',k'} \times(\rho)d\phi rdrdz\sim\delta_{m,m'},$$

from where the conservation of the m number is immediately obtained: $m=m'$.

In Table I we show the mapping between the notation of the hole states used previously n_v and the (m,k) notation. A similar table can be drawn for the electron states. As an example, the nondiagonal optical transition (14) shown both in Fig. 4 or Fig. 5 is relatively strong because both the first electron state (1) and the fourth hole state (4) have the same m quantum number, i.e., $m=0$.

B. Rectangular micromagnet: A one-dimensional trap

In this section we consider a rectangular, flat Fe micromagnet in the single-domain state,[19] with magnetization pointing in the x direction.[9,10,22] The single-domain state of the micromagnet with the mentioned size was investigated by micromagnetic simulations using the OOMMF package.[23] Without an external magnetic field the sample does not remain as an ordered single domain, but goes into a multidomain structure instead. The simulations show, however, that after magnetizing the sample with a field of 1 T and reducing the field close to 0 T, a value of 0.2 T is sufficient to restore a state that—for our purposes—is sufficiently close to a single domain. Because of the magnetic anisotropy of the g_h, this additional field is unimportant for electrons in the valence band, but it does have a slight effect on the conduction electron spectrum.

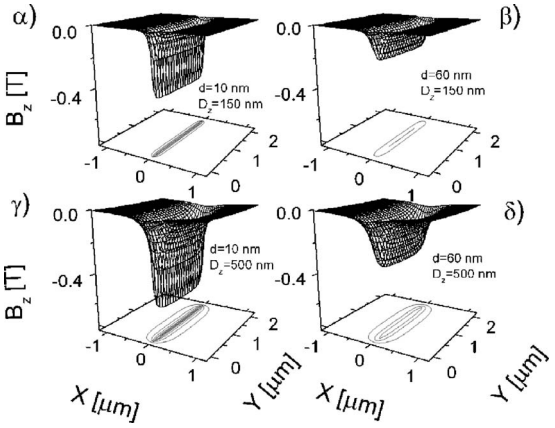

FIG. 6. Z component of the magnetic field $\vec{B}$ produced by a rectangular micromagnet at a distance d below its narrow edge. We show results for two distances, $d=10$ nm and $d=60$ nm, and for two micromagnet thicknesses, $D_z=150$ nm and $D_z=500$ nm. Contour plots on the xy planes indicate localization and "strength" of the z component of the magnetic field.

In Fig. 6 we present the z component of the magnetic field below one of the two poles of the micromagnet ($D_x=6$ μm $\times D_y=2$ μm$\times D_z$, see inset in Fig. 7). The thickness D_z is a parameter in our simulations, and we vary this value in the range from 150 to 500 nm. For large D_x, the local magnetic field $\vec{B}(\vec{r})$ can be thought to be a sum of two fields (one of them is shown in Fig. 6) produced by the magnetic charges localized at the two magnetic poles of the micromagnet. The magnetic field B_z on the second pole has an opposite direction to this field, and thus "attracts" quasiparticles with the opposite spin. The top two plots (α and β) in Fig. 6 are for two different distances, $d=10$ nm and $d=60$ nm, keeping a constant thickness of $D_z=150$ nm. The two bottom plots (γ and δ) are for the same distances, using $D_z=500$ nm. When the distance d is increased while keeping the thickness D_z constant (as we go from α to β or from γ to δ), the magnetic field B_z is seen to decrease, as expected. In contrast, when the thickness D_z increases for a constant d ($\alpha\rightarrow\gamma$ or $\beta\rightarrow\delta$), the magnetic field B_z is seen to increase. This suggests that, by depositing thicker micromagnets, larger magnetic fields can be produced for the same separation between the micromagnet and the QW. In Fig. 6, we also show contour plots of B_z on the XY plane, which indicate the spatial extent of the magnetic field and its gradient. In all cases (α, β, γ, and δ), we see that B_z is confined to a narrow region in the x direction and is delocalized in the y direction over the distance of

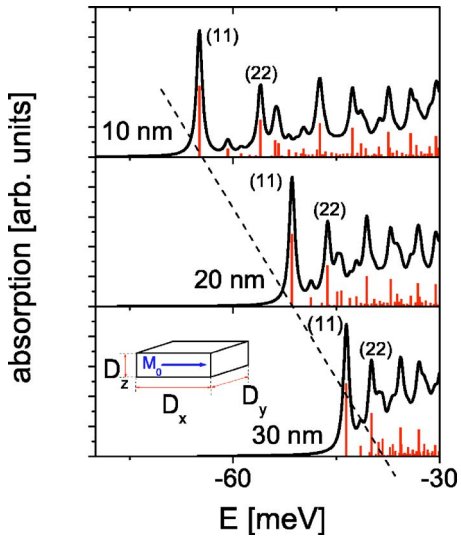

FIG. 7. (Color online) Absorption coefficient for distances $d=10$, 20, and 30 nm (from top to bottom) between the rectangular micromagnet ($D_z=150$ nm, $D_x=6$ μm, and $D_y=2$ μm) and the QW. The binding energy as well as the separation between the peaks decreases almost linearly with increasing d. In the inset we show the arrangement of the rectangular micromagnet in a single domain state. Magnetization is pointing in the x direction.

two microns. With increasing thickness D_z ($\alpha \rightarrow \gamma$ or $\beta \rightarrow \delta$) the "spread" of B_z in the x direction is seen to increase.

Our calculations show that at $d=10$ nm ($D_z=150$ nm), the maximum value of the magnetic field is $|\vec{B}|_{max}=0.6$ T. This value is larger than for a microdisk because in the present case the thickness of the rectangular micromagnet is larger. We must emphasize that the gradient of the magnetic field[24] is as large as 2 mT/Å for $d=10$ nm, so that a precise determination of $|\vec{B}|_{max}$ or of the magnetic field profile is challenging even in the simple case of a single-domain phase.

In Fig. 7 we present the absorption spectrum at three distances d between the QW and the micromagnet: $d=10$, 20, and 30 nm. In all three cases the thickness of the micromagnet was kept at a constant value of $D_z=150$ nm. As before, we chose the zero of the energy axis at the main absorption peak. At $d=10$ nm, the binding energy is 66 meV, while at $d=60$ nm it is smaller by a factor of 2. This follows from the fact that the further the micromagnet is from the QW, the smaller is the magnetic field at the QW position (see also Fig. 6). Nondiagonal transitions are relatively strong both in the case of the microdisk and of the rectangular micromagnet.[10] The separation between the peaks decreases as d increases, because the gradient of the magnetic field (and equivalently, the gradient of the potential) also decreases with increasing d.

In Fig. 8 we show the behavior of the absorption coefficient for three thicknesses $D_z=100$, 200, and 300 nm, for the same micromagnet-QW distance d. With increasing D_z, the binding energy increases almost linearly. This is seen in Fig. 8 as a linear shift of the (11) transition. An interesting observation is that the separation between the peaks does not depend on D_z in the range 100–300 nm and for the parameters that we have used. As in the previous paragraphs the pair

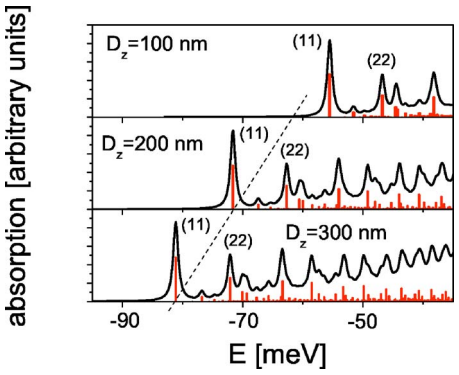

FIG. 8. (Color online) Absorption coefficient for different thicknesses D_z of a rectangular micromagnet. In this case the distance between the micromagnet and the QW is constant, $d=10$ nm. Separation between peaks is barely distinguishable for all three D_z values. Note that the absorption peak (11) shifts almost linearly with D_z.

($n_c n_v$) denotes transition between the n_v^{th} hole state and the n_c^{th} electron state. Contrary to the disk case, for the rectangular micromagnet only (odd, odd) or (even, even) transitions are allowed, see Fig. 9.

Let us now return to the anisotropy of the g factor of the holes that was described in Sec. II. In Fig. 9 we compare the absorption spectrum calculated for the two approximations: the isotropic and the anisotropic cases of the g_h factor. As an example we have chosen the rectangular micromagnet for discussing the magnetic anisotropy of the QW. The electron g factor is isotropic in both cases. We see that, at least in the low energy region, the two spectra are the same: the position of the transition energies as well as the oscillator strengths are nearly the same for both g factor models. Thus, for the arrangement discussed in this work (see inset in Fig. 7) and for the geometrical parameters we have used (such as the size and the shape of the magnets), only the z component of the magnetic field produced by the micromagnet is important.

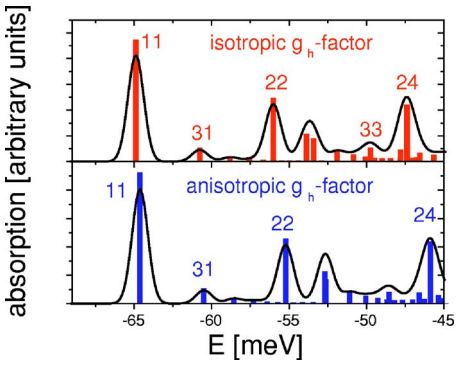

FIG. 9. (Color online) Comparison of the absorption spectrum in two models: the isotropic and the anisotropic g factor of the hole. The electron g factor is isotropic. The top and bottom spectra are very similar. Calculations done for rectangular Fe micromagnet with dimensions of $D_x=6$ μm, $D_y=2$ μm, $D_z=0.15$ μm on the top of a QW structure at a distance $d=10$ nm apart.

IV. CONCLUSIONS

We analyzed theoretically the optical response of a hybrid structure composed of a micromagnet deposited on top of a diluted magnetic semiconductor quantum well structure. While we focused on calculating the absorption coefficient, directly measurable in an optical absorption experiment, the results of this paper are equally well suited for predicting the outcome of a photoluminescence experiment.

The calculations were performed for two types of ferromagnetic micromagnets: a cylindrical microdisk and a rectangular micromagnet. We analyzed the local magnetic field produced by the micromagnets. In the case of a microdisk, the magnetic field, together with the QW confinement potential, traps the quasiparticle (e.g., an exciton) in all three spatial directions. However, a rectangular micromagnet traps quasiparticles only in two spatial directions, allowing them to behave as one-dimensional quasiparticles. We described the approximations we used in our approach, including a discussion of the anisotropy of the g factor of the hole states. Then we calculated the absorption coefficients for both shapes of the micromagnets for various micromagnet-QW separations and micromagnet thicknesses.

In order to observe zero-dimensional and one-dimensional states inside the DMS QW it is necessary to produce as strong a local magnetic field as possible. This can be achieved, for example, by utilizing materials with high saturation magnetization. Our analysis shows that it is better to deposit a thicker ferromagnetic layer, since thicker micromagnets produce a stronger local magnetic field. As expected, the growth of a high quality QW relatively close to the interface between the micromagnetic and the semiconductor is of major importance for optimal quasiparticle localization. Since high values of g factors are of critical importance for fabricating efficient spin traps, optical localization is most likely expected to be observed in DMS-based quantum structures at low temperature.

Finally, since quasi-one-dimensional states emerge only below the poles of the rectangular micromagnet and zero-dimensional states emerge only below the center of the disk, spatially resolved techniques such as microphotoluminescence, microreflectance, or near-field scanning optical microscopy are preferred for observing the effects presented in this paper. Since both zero-dimensional and one-dimensional states are spin polarized, unambiguous identification of the confined states requires the use of polarization sensitive techniques. Specifically, in the case of a rectangular micromagnet the states created underneath the opposite poles should have opposite spin-polarization, which can serve as a convincing test of the appearance of these new states.

ACKNOWLEDGMENTS

This research was supported by the National Science Foundation under NSF-NIRT Grant No. DMR 02-10519; by the U.S. Department of Energy, Basic Energy Sciences, under Contract No. W-7405-ENG-36; and by the Alfred P. Sloan Foundation (B. J.).

[1] H. Ohno, F. Matsukura, and Y. Ohno, Japan Society of Applied Physics **5**, 4 (2002).
[2] D. Grundler, T. M. Hengstmann, and H. Rolff, Braz. J. Phys. **34**, 598 (2004).
[3] S. Kreuzer, M. Rahm, J. Bigerger, R. Pulwey, J. Raabe, D. Schuh, W. Wegscheider, and D. Weiss, Physica E (Amsterdam) **16**, 137 (2003).
[4] P. Kossacki, J. Cibert, D. Ferrand, Y. Merle d'Aubigné, A. Arnoult, A. Wasiela, S. Tatarenko, and J. A. Gaj, Phys. Rev. B **60**, 16018 (1999).
[5] M. Combescot, O. Betbeder-Matibet, and F. Dubin, Eur. Phys. J. B **42**, 63 (2004).
[6] J. A. K. Freire, F. M. Peeters, A. Matulis, V. N. Freire, and G. A. Farias, Phys. Rev. B **62**, 7316 (2000).
[7] M. Berciu and B. Jankó, Phys. Rev. Lett. **90**, 246804 (2003).
[8] J. Kossut, I. Yamakawa, A. Nakamura, G. Cywiński, K. Fronc, M. Czeczott, J. Wróbel, F. Kyrychenko, T. Wojtowicz, and S. Takeyama, Appl. Phys. Lett. **79**, 1789 (2001).
[9] G. Cywiński, M. Czeczott, J. Wróbel, K. Fronc, A. Aleszkiewicz, S. Maćkowski, T. Wojtowicz, and J. Kossut, Physica E (Amsterdam) **13**, 560 (2002).
[10] P. Redliński, T. Wojtowicz, T. G. Rappoport, A. Libál, J. K. Furdyna, and B. Jankó, Appl. Phys. Lett. **86**, 113103 (2005).
[11] M. Berciu, T. G. Rappoport, and B. Janko, Nature (London) **435**, 71 (2005).
[12] J. K. Furdyna, J. Appl. Phys. **64**, R29 (1988).
[13] J. K. Furdyna and J. Kossut, *Diluted Magnetic Semiconductors* (Academic, Boston, 1988).
[14] T. Dietl, M. Sawicki, M. Dahl, D. Heiman, E. D. Isaacs, M. J. Graf, S. I. Gubarev, and D. L. Alov, Phys. Rev. B **43**, 3154 (1991).
[15] B. Kuhn-Heinrich, W. Ossau, H. Heinke, F. Fischer, T. Liz, A. Waag, and G. Landwehr, Appl. Phys. Lett. **63**, 2932 (1993).
[16] O. Madelung, *Introduction to Solid-State Theory*, 3rd ed. (Springer, New York, 1996).
[17] J. M. Luttinger and W. Kohn, Phys. Rev. **97**, 869 (1955).
[18] M. Abolfath, T. Jungwirth, J. Brum, and A. H. MacDonald, Phys. Rev. B **63**, 054418 (2001).
[19] J. D. Jackson, *Classical Electrodynamics*, xxi ed. (Wiley, New York, 1999).
[20] B. Kuhn-Heinrich, W. Ossau, E. Bangert, A. Waag, and G. Landwehr, Solid State Commun. **91**, 413 (1994).
[21] J. K. Ha, R. Hertel, and J. Kirschner, Phys. Rev. B **67**, 224432 (2003).
[22] P. A. Crowell, V. Nikitin, D. D. Awschalom, F. Flack, N. Samarth, and G. A. Prinz, J. Appl. Phys. **81**, 5441 (1997).
[23] See http://math.nist.gov/oommf/, OOMMF User's Guide, Version 1.0, M. J. Donahue and D. G. Porter, Interagency Report NISTIR 6376, National Institute of Standards and Technology Gaithersburg, MD (Sept. 1999).
[24] F. Pulizzi, P. C. M. Christianen, J. C. Maan, T. Wojtowicz, G. Karczewski, and J. Kossut, Phys. Status Solidi A **178**, 33 (2000).